

Dynamic Memory-enhanced Transformer for Hyperspectral Image Classification

Muhammad Ahmad, Manuel Mazzara, Salvatore Distefano, Adil Mehmood Khan

Abstract—Hyperspectral image (HSI) classification remains a challenging task due to the intricate spatial-spectral correlations. Existing transformer models excel in capturing long-range dependencies but often suffer from information redundancy and attention inefficiencies, limiting their ability to model fine-grained relationships crucial for HSI classification. To overcome these limitations, this work proposes MemFormer, a lightweight and memory-enhanced transformer. MemFormer introduces a memory-enhanced multi-head attention mechanism that iteratively refines a dynamic memory module, enhancing feature extraction while reducing redundancy across layers. Additionally, a dynamic memory enrichment strategy progressively captures complex spatial and spectral dependencies, leading to more expressive feature representations. To further improve structural consistency, we incorporate a spatial-spectral positional encoding (SSPE) tailored for HSI data, ensuring continuity without the computational burden of convolution-based approaches. Extensive experiments on benchmark datasets demonstrate that MemFormer achieves superior classification accuracy, outperforming state-of-the-art methods.

Index Terms—Hyperspectral Image Classification; Memory Enhanced Attention; Transformer.

I. INTRODUCTION

HYPERSPECTRAL IMAGING has become a powerful tool in various applications, offering detailed spectral information across hundreds of contiguous bands. This rich data enables fine-grained material classification [1], [2]. However, deploying hyperspectral image classification (HSIC) models in real-world scenarios remains challenging due to spectral variability, complex spatial structures, and the Hughes phenomenon [3]. To be effective, classification frameworks must strike a balance between high accuracy, computational efficiency, and the ability to capture spatial-spectral dependencies [4] jointly.

In recent years, transformer-based models have achieved remarkable success in HSIC by leveraging self-attention to process image patches directly. For example, Huang et al. [5] introduced SS-VFMT, a spectral-spatial transformer that enhances pre-trained vision foundation models (VFMs) with dedicated spectral and spatial modules. Zhao et al. [6] proposed GSC-ViT, which integrates GroupWise separable convolution (GSC) and multi-head self-attention (GSSA) to im-

prove feature extraction efficiency. Similarly, Ahmad et al. [7] developed SSFormer, incorporating implicit conditional PEs to enable flexible input adaptation. While these approaches enhance spectral-spatial modeling, they often face limitations such as high computational costs, dependence on pre-trained models, and difficulties in adapting to domain-specific variations.

Hybrid architectures, such as CNN-transformer fusion models, aim to bridge the gap between local and global feature extraction. For instance, Yu et al. [8] introduced Hypersinet, a cross-attention fusion network that integrates CNNs and transformers, while Ahmad et al. [9] proposed WaveFormer, which replaces traditional pooling operations with wavelet transforms for more effective downsampling. Although these methods enhance feature representation, their hybrid design comes at the cost of increased training complexity and computational demands.

Other approaches, including PyFormer [10], CMT [11], DiffFormer [12], and MASSFormer [13], employ hierarchical or memory-based architectures to refine feature extraction. However, these models often introduce additional design complexities, require extensive parameter tuning, and struggle to capture fine-grained spatial-spectral relationships in high-dimensional HSI data.

Zhang et al. [14] proposed the Tensor Transformer (TT) framework, which enhances HSIC by preserving spatial-spectral integrity through a Tensor Self-Attention Mechanism (TSAM), eliminating the need for sequentialization. While this approach improves long-range feature extraction, direct tensor operations may increase computational complexity. Unlike MemFormer, which refines features using memory-enhanced attention, TT focuses on maintaining structural relationships without explicitly addressing redundancy.

Similarly, Wang et al. [15] introduced a mixed CNN-transformer network with graph contrastive learning (MCT-GCL) to improve Mars HSIC. This model combines CNNs for local feature extraction with transformers for global modeling while minimizing complexity through a lightweight dual-branch design. It further enhances inter-class discrimination using graph contrastive learning and introduces the HyMars dataset for validation. However, while optimized for planetary HSI, its applicability to Earth observation remains limited.

Despite significant progress in transformer-based HSIC, several key challenges remain: **Local vs. Global Feature Extraction Trade-off**: Many existing models struggle to balance local and global feature extraction [16]. CNN-based models are constrained by limited receptive fields, whereas transformer architectures often introduce redundancy and information loss in multi-head self-attention (MHSA) mecha-

M. Ahmad is with SDAIA-KFUPM, Joint Research Center for Artificial Intelligence (JRCAI), King Fahd University of Petroleum and Minerals, Dhahran, 31261, Saudi Arabia. (e-mail: mahmad00@gmail.com).

S. Distefano is with the Dipartimento di Matematica e Informatica—MIFT, University of Messina, Messina 98121, Italy. (e-mail: sdistefano@unime.it).

M. Mazzara is with the Institute of Software Development and Engineering, Innopolis University, Innopolis, 420500, Russia. (e-mail: m.mazzara@innopolis.ru)

A.M. Khan is with the School of Computer Science, University of Hull, Hull HU6 7RX, UK. (e-mail: a.m.khan@hull.ac.uk)

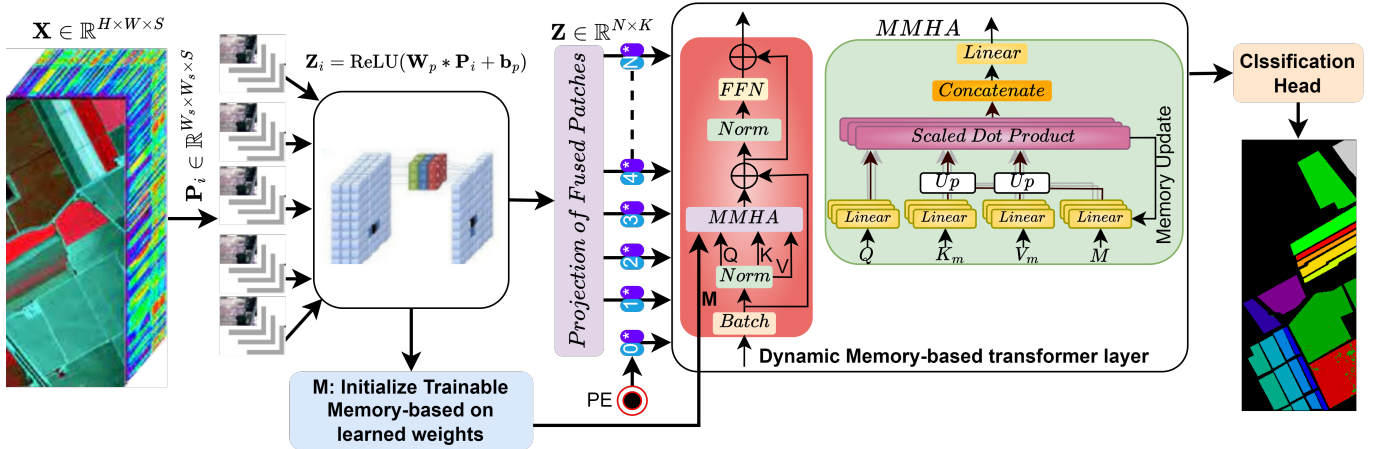


Fig. 1: Overall architecture of dynamic memory-enhanced MHSA mechanism-based spatial-spectral transformer for HSIC.

nisms [17], [18]. **Computational Complexity:** Transformer-based methods tend to be memory-intensive and computationally inefficient, making scalability a challenge [19], [20]. **Spectral-Spatial Information Blending:** Cross-domain transfer learning models often fail to effectively preserve spectral and spatial information, leading to suboptimal domain adaptation performance [21]. **Memory-Based Representations and Overhead:** While memory tokens and multi-scale attention mechanisms can enhance feature extraction, they often introduce additional complexity and increase the risk of overfitting in high-dimensional settings [22]. Given these limitations, there is a need for a model that (1) effectively balances local and global feature extraction without excessive redundancy, (2) preserves spectral-spatial relationships without introducing artifacts from positional encoding (PE), and (3) generalizes well across datasets with diverse spectral and spatial characteristics.

To address these challenges, this work proposes MemFormer (MSST), a dynamic memory-enhanced transformer designed to seamlessly integrate spectral and spatial information while mitigating the drawbacks of conventional transformer-based models. MemFormer achieves a superior balance between accuracy, computational efficiency, and feature representation by introducing memory-enhanced attention, adaptive memory refinement, and an efficient spectral-spatial encoding strategy. The key contributions are as follows:

Memory-enhanced MHSA with Dynamic Refinement: MemFormer incorporates a memory-enhanced attention mechanism that integrates a dynamically evolving memory module into MHSA. Unlike standard MHSA, which suffers from redundancy and information dilution, our dynamic memory component iteratively refines itself across layers, capturing and propagating long-range contextual dependencies. Additionally, MemFormer updates this memory dynamically during inference, allowing attention outputs to iteratively enrich spectral-spatial representations. This enhances information flow, mitigates spectral-spatial information decay, and improves feature expressiveness, particularly in heterogeneous environments where feature dependencies evolve across scales. **Spatial-Spectral PE (SSPE) for Structure Preservation:** To maintain

structural integrity, we introduce a SSPE scheme tailored to spectral-spatial characteristics. This encoding efficiently models spectral continuity and spatial dependencies, enabling effective local-global feature aggregation.

II. PROPOSED METHODOLOGY

Let the input HSI be denoted as $\mathbf{X} \in \mathbb{R}^{H \times W \times S}$, where H and W are the spatial dimensions, and S is the number of spectral bands. To process the data efficiently, the HSI is divided into N non-overlapping patches, each of size $W_s \times W_s \times S$. A patch is denoted by $\mathbf{P}_i \in \mathbb{R}^{W_s \times W_s \times S}$, for $i = 1, 2, \dots, N$, where $N = \frac{H \times W}{W_s^2}$. This patch-wise tokenization preserves local spatial-spectral information and reduces computational complexity. Each patch is mapped to a lower-dimensional feature vector via a 2D convolutional layer:

$$\mathbf{Z}_i = \text{ReLU}(\mathbf{W}_p * \mathbf{P}_i + \mathbf{b}_p) \quad (1)$$

where $\mathbf{W}_p \in \mathbb{R}^{K \times W_s \times W_s \times S}$ is the learnable kernel, K is the embedding dimension, and $*$ denotes the convolution operation. After transformation, all patch embeddings are concatenated into a matrix $\mathbf{Z} \in \mathbb{R}^{N \times K}$.

A. Spatial-Spectral Positional Embedding (SSPE)

To preserve both the spatial layout and spectral order, we define a spatial-spectral positional embedding (SSPE). Let (x_i, y_i) denote the 2D coordinates of patch i , and s_j the spectral band index. The spatial encoding uses separate sinusoidal functions along each axis:

$$E_x(x_i, 2j) = \sin\left(\frac{x_i}{\lambda^{2j/d}}\right), \quad E_x(x_i, 2j+1) = \cos\left(\frac{x_i}{\lambda^{2j/d}}\right) \quad (2)$$

$$E_y(y_i, 2j) = \sin\left(\frac{y_i}{\lambda^{2j/d}}\right), \quad E_y(y_i, 2j+1) = \cos\left(\frac{y_i}{\lambda^{2j/d}}\right) \quad (3)$$

where λ is a wavelength parameter and d is the embedding size. The combined spatial embedding is:

$$E_{\text{spatial}}(x_i, y_i) = [E_x(x_i); E_y(y_i)] \in \mathbb{R}^{K_s} \quad (4)$$

Similarly, the spectral embedding is defined as:

$$E_{\text{spectral}}(s_j, 2k) = \sin\left(\frac{s_j}{\gamma^{2k/d}}\right) \quad (5)$$

$$E_{\text{spectral}}(s_j, 2k + 1) = \cos\left(\frac{s_j}{\gamma^{2k/d}}\right) \quad (6)$$

resulting in $E_{\text{spectral}}(s_j) \in \mathbb{R}^{K_\sigma}$. To ensure compatibility, we project both spatial and spectral encodings to the same dimension K via learnable linear layers:

$$E_{\text{SSPE}} = \text{MLP}([\text{Proj}_s(E_{\text{spatial}}); \text{Proj}_\sigma(E_{\text{spectral}})]) \in \mathbb{R}^{N \times K} \quad (7)$$

where $\text{Proj}_s: \mathbb{R}^{K_s} \rightarrow \mathbb{R}^K$ and $\text{Proj}_\sigma: \mathbb{R}^{K_\sigma} \rightarrow \mathbb{R}^K$. The SSPE allows the model to encode both spatial identity and spectral continuity, addressing the challenge of distinguishing patches located at different positions but sharing similar spectra.

B. Dynamic Memory Attention

We enhance traditional attention with a global memory mechanism to capture long-range dependencies. A classification token $\mathbf{z}_{\text{CLS}} \in \mathbb{R}^K$ is prepended to the embedding sequence, and SSPE is added:

$$\mathbf{Z}' = [\mathbf{z}_{\text{CLS}}; \mathbf{Z}] + E_{\text{SSPE}} \quad (8)$$

Let the query matrix be $\mathbf{Q} \in \mathbb{R}^{B \times N \times K}$ for a batch of size B . We maintain a global dynamic memory matrix $\mathbf{M} \in \mathbb{R}^{M \times K}$, where M is the memory length. This memory is not trainable but dynamically updated per batch via a First-In-First-Out (FIFO)¹ policy to retain recent global features. The memory is tiled across batches: $\mathbf{K}_m = \mathbf{V}_m = \text{Tile}(\mathbf{M}, B) \in \mathbb{R}^{B \times M \times K}$. Memory-based attention is computed as:

$$\mathbf{A} = \text{Softmax}\left(\frac{\mathbf{Q}\mathbf{K}_m^\top}{\sqrt{K}}\right)\mathbf{V}_m \quad (9)$$

The result is normalized via residual connection:

$$\mathbf{A}' = \text{LayerNorm}(\mathbf{Q} + \mathbf{A}) \quad (10)$$

To update the memory, we compute the mean over batch and token dimensions:

$$\mathbf{m}_{\text{new}} = \frac{1}{B} \sum_{b=1}^B \left(\frac{1}{N} \sum_{n=1}^N \mathbf{A}[b, n, :] \right) \quad (11)$$

and append it to memory by discarding the oldest entry:

$$\mathbf{M} \leftarrow [\mathbf{M}[1 :, :]; \mathbf{m}_{\text{new}}] \quad (12)$$

The memory-tiled keys and values are recomputed with updated memory as:

$$\mathbf{K}_m^{\text{updated}} = \mathbf{V}_m^{\text{updated}} = \text{Tile}(\mathbf{M}, B) \quad (13)$$

¹FIFO is a memory management strategy where the oldest stored elements are removed first when new elements are added, ensuring that the memory retains the most recent information while discarding outdated entries.

with $\mathbf{K}_m^{\text{updated}}, \mathbf{V}_m^{\text{updated}} \in \mathbb{R}^{B \times M \times K}$. The final attention output is then recomputed as:

$$\mathbf{A}_{\text{final}} = \text{Softmax}\left(\frac{\mathbf{Q}\mathbf{K}_m^{\text{updated}\top}}{\sqrt{K}}\right)\mathbf{V}_m^{\text{updated}} \quad (14)$$

This final output is normalized:

$$\mathbf{A}'_{\text{final}} = \text{LayerNorm}(\mathbf{Q} + \mathbf{A}_{\text{final}}) \quad (15)$$

C. Feedforward Network and Classification

A position-wise feedforward network (FFN) enhances non-linearity:

$$\text{FFN}(\mathbf{X}) = \text{ReLU}(\mathbf{X}\mathbf{W}_1 + \mathbf{b}_1)\mathbf{W}_2 + \mathbf{b}_2 \quad (16)$$

where $\mathbf{W}_1 \in \mathbb{R}^{K \times D}$, $\mathbf{W}_2 \in \mathbb{R}^{D \times K}$, and D is the hidden dimension. The final embedding is:

$$\mathbf{Z}'' = \text{LayerNorm}(\mathbf{A}'_{\text{final}} + \text{FFN}(\mathbf{A}'_{\text{final}})) \quad (17)$$

The FFN introduces non-linearity and refines features, crucial for accurate classification. The classification is performed using the CLS token:

$$\mathbf{z}_{\text{CLS}}^{\text{final}} = \mathbf{Z}''[0, :] \quad (18)$$

$$\mathbf{y} = \text{Softmax}(\mathbf{z}_{\text{CLS}}^{\text{final}}\mathbf{W}_c + \mathbf{b}_c) \quad (19)$$

where $\mathbf{W}_c \in \mathbb{R}^{K \times C}$ and C is the number of classes.

III. ABLATION STUDY

This section presents a detailed ablation study to highlight the contribution of individual components in our proposed model. The experiments are conducted on three benchmark HSI datasets: Indian Pines (IP), WHU-Hi-HanChuan (HC), and WHU-Hi-HongHu (HH). We specifically focus on the effect of (1) Memory Attention, (2) various PE strategies, and (3) tokens in the memory.

To evaluate the contribution of the Memory Attention module, we compare its performance against the standard self-attention mechanism. Table I shows the results across all three datasets. As shown in Table I, the inclusion of the Memory Attention mechanism significantly improves the classification performance across all metrics. Notably, the κ coefficient and OA show substantial gains of over 4% on the IP dataset and nearly 2% on HC and HH. This validates that incorporating memory mechanisms into attention helps retain important contextual information, which is especially beneficial in HSI where spatial-spectral dependencies are crucial.

TABLE I: Impact of Memory Attention (✓) and Standard Attention (✗).

| Attention | IP | | | HC | | | HH | | |
|-----------|----------------|----------------|----------------|----------------|----------------|----------------|----------------|----------------|----------------|
| | κ | OA | AA | κ | OA | AA | κ | OA | AA |
| ✗ | 94.9254 | 95.5512 | 95.5071 | 97.2897 | 97.6849 | 95.5937 | 96.2205 | 97.0084 | 92.8485 |
| ✓ | 99.4882 | 99.5512 | 99.3822 | 99.1413 | 99.2661 | 98.6722 | 98.1217 | 98.5140 | 97.2595 |

To further understand the effectiveness of our SSPE, we compare it with three alternatives: (i) No PE, (ii) Sinusoidal

TABLE II: Impact of Different PE Mechanisms on Model Performance.

| PE | IP | | | HC | | | HH | | |
|------------|----------------|----------------|----------------|----------------|----------------|----------------|----------------|----------------|----------------|
| | κ | OA | AA | κ | OA | AA | κ | OA | AA |
| None | 98.2214 | 98.4132 | 97.8479 | 98.0047 | 98.3620 | 96.5096 | 97.5590 | 97.9047 | 95.1268 |
| Learnable | 98.7449 | 98.9020 | 98.3017 | 98.5491 | 98.7615 | 97.3640 | 97.9915 | 98.3311 | 95.8822 |
| Sinusoidal | 98.5311 | 98.7204 | 98.0896 | 98.3622 | 98.6405 | 97.1124 | 97.8120 | 98.1905 | 95.6381 |
| SSPE | 99.0143 | 99.1065 | 99.7213 | 98.8728 | 99.0124 | 98.9257 | 98.2673 | 98.6072 | 97.7714 |

encoding, (iii) Learnable encoding, and (iv) SSPE. The results are summarized in Table II. From Table II, we observe that the absence of any PE leads to a performance drop, especially in AA, indicating the importance of encoding position in spatial-spectral analysis. While both sinusoidal and learnable PEs provide moderate improvements, the proposed SSPE consistently outperforms all alternatives across datasets. This highlights the importance of integrating domain-aware spatial and spectral cues into the model’s attention mechanism.



Fig. 2: Effect of memory size on OA.

Figure 2 explores the sensitivity of the model to different memory sizes, expressed as the number of tokens preserved in memory. The results indicate that a memory size of 10 tokens consistently provides optimal or near-optimal OA for all datasets. While very small memory sizes (e.g., 1 token) fail to retain sufficient context, excessively large memory sizes (e.g., 25 or 30 tokens) may introduce noise or redundancy, leading to marginal degradation or plateauing in performance. These trends underline the need for a balanced memory configuration that preserves informative context without overwhelming the attention mechanism.

IV. COMPARATIVE RESULTS AND DISCUSSION

To evaluate the effectiveness of our proposed MemFormer (MSST), we compare it against state-of-the-art methods, including 2D CNN [23], 3D CNN [24], Hybrid CNN (HCNN) [25], Pyramid Transformer (PF) [10], WaveFormer (WF) [9], Hyperspectral Spatial-Spectral Transformer (HSST) [8], and Spectral-Spatial Transformer (SST) [26]. The experimental settings ensure a fair comparison, with a consistent patch size (14) and feature dimension ($K = 15$). The dataset is split into 25% training and validation and 50% testing (stratified sampling with cross-validation). Models are trained for 50 epochs using the Adam optimizer with a learning rate of 0.001 and weight decay of 10^{-6} . The transformer-based architectures are configured with 4 layers, 8 attention heads, and a dropout rate of 0.1, ensuring computational efficiency. The training dynamics of all competing methods are presented in Fig. 3.

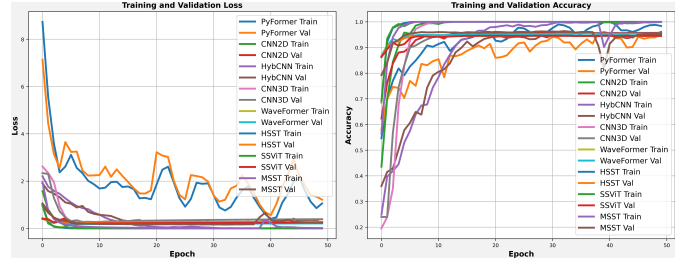


Fig. 3: Training and validation accuracy and loss curves for all competing methods. The figure illustrates the convergence behavior and generalization performance of each model across training epochs.

TABLE III: IP Dataset: Per-class classification results, along with OA, AA, and κ .

| Class | 2DCNN [23] | HCNN [25] | 3DCNN [24] | HSST [8] | SST [26] | PF [10] | WF [9] | MSST |
|-----------|-----------------|----------------|-----------------|-----------------|-----------------|-----------------|-----------------|-----------------|
| 1 | 56.5217 | 60.8695 | 73.9130 | 69.5652 | 100.0000 | 91.3043 | 91.3043 | 95.6521 |
| 2 | 93.8375 | 97.3389 | 93.9775 | 92.0168 | 92.4369 | 95.2380 | 92.2969 | 99.2997 |
| 3 | 96.6265 | 96.3855 | 96.6265 | 95.6626 | 96.3855 | 91.5662 | 96.8674 | 100.0000 |
| 4 | 85.5932 | 90.6779 | 83.0508 | 94.0677 | 92.3728 | 89.8305 | 86.4406 | 100.0000 |
| 5 | 96.2809 | 97.5206 | 95.0413 | 99.1735 | 97.5206 | 96.2809 | 97.1074 | 97.5206 |
| 6 | 98.6301 | 99.7260 | 99.4520 | 99.1780 | 98.9041 | 98.6301 | 98.9041 | 99.1780 |
| 7 | 100.0000 | 71.4255 | 92.8571 | 100.0000 | 100.0000 | 92.8571 | 100.0000 | 100.0000 |
| 8 | 100.0000 | 99.5815 | 99.5815 | 100.0000 | 100.0000 | 100.0000 | 100.0000 | 100.0000 |
| 9 | 60.0000 | 50.0000 | 100.0000 | 90.0000 | 80.0000 | 90.0000 | 80.0000 | 100.0000 |
| 10 | 90.9465 | 95.6790 | 91.9753 | 86.8312 | 87.6543 | 89.5061 | 85.1851 | 99.3827 |
| 11 | 96.8241 | 98.8599 | 97.3127 | 96.3355 | 96.8241 | 98.0456 | 96.9055 | 99.7557 |
| 12 | 96.2962 | 96.6329 | 91.2457 | 90.9090 | 94.2760 | 92.2558 | 88.2154 | 99.3265 |
| 13 | 97.0588 | 97.0588 | 99.0196 | 100.0000 | 99.0196 | 100.0000 | 100.0000 | 100.0000 |
| 14 | 99.2101 | 99.0521 | 98.8941 | 98.5781 | 98.4202 | 99.0521 | 97.7883 | 100.0000 |
| 15 | 95.8549 | 83.4196 | 93.2642 | 97.4093 | 94.3005 | 97.4093 | 97.9274 | 100.0000 |
| 16 | 100.0000 | 93.4782 | 100.0000 | 100.0000 | 100.0000 | 93.4782 | 100.0000 | 100.0000 |
| Para | 1078336 | 1380480 | 15808224 | 836816 | 836816 | 16680662 | 2667408 | 847632 |
| Train (s) | 24.03 | 30.83 | 40.96 | 102.46 | 106.02 | 1019.90 | 96.38 | 101.64 |
| Test (s) | 0.90 | 0.83 | 0.78 | 2.37 | 2.33 | 12.92 | 2.48 | 2.34 |
| Flops | 2670080 | 18778112 | 15732736 | 110592 | 110592 | 15730688 | 167936 | 3108864 |
| κ | 95.2557 | 96.4373 | 95.1454 | 94.5476 | 94.9254 | 95.2985 | 94.1671 | 99.4882 |
| OA | 95.8439 | 96.8780 | 95.7463 | 95.2195 | 95.5512 | 95.8829 | 94.8878 | 99.5512 |
| AA | 91.4800 | 89.2318 | 94.1382 | 94.3579 | 95.5071 | 94.7159 | 94.3089 | 99.3822 |

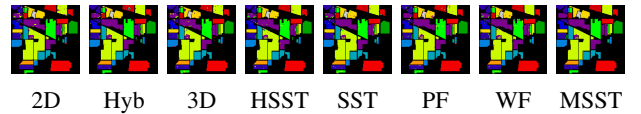


Fig. 4: IP dataset: Classification maps, highlighting spatial variability and class-specific performance.

TABLE IV: HC Dataset: Per-class classification results, along with OA, AA, and κ .

| Class | 2DCNN [23] | HCNN [25] | 3DCNN [24] | HSST [8] | SST [26] | PF [10] | WF [9] | MSST |
|-----------|------------|-----------|----------------|----------------|----------|----------------|---------|----------------|
| 1 | 98.3234 | 98.7169 | 98.8286 | 98.5693 | 99.1416 | 98.4218 | 98.7705 | 99.4501 |
| 2 | 98.7167 | 96.8620 | 97.9607 | 96.8445 | 97.4334 | 98.0311 | 98.884 | 99.7011 |
| 3 | 95.8584 | 98.3667 | 97.4722 | 97.8417 | 97.9972 | 99.4166 | 95.1390 | 99.9611 |
| 4 | 99.5143 | 99.4023 | 99.0661 | 99.8879 | 99.5143 | 95.6667 | 98.2069 | 99.2528 |
| 5 | 92.5000 | 96.1666 | 98.3333 | 97.0000 | 97.0000 | 94.0000 | 89.1666 | 99.1666 |
| 6 | 80.1412 | 89.7175 | 95.4986 | 80.2736 | 87.5551 | 67.5639 | 84.4218 | 93.2480 |
| 7 | 93.6991 | 98.2723 | 97.3238 | 97.0867 | 94.6476 | 90.3794 | 92.8184 | 98.8143 |
| 8 | 95.0828 | 86.7393 | 98.1087 | 95.2386 | 96.0841 | 94.1039 | 95.4611 | 98.0976 |
| 9 | 97.3806 | 96.6201 | 97.5496 | 94.2120 | 97.0849 | 96.2822 | 93.3248 | 98.4579 |
| 10 | 98.4024 | 99.5625 | 99.2963 | 98.2312 | 98.3453 | 99.9239 | 98.7828 | 99.6386 |
| 11 | 98.6162 | 98.9710 | 99.5742 | 97.8829 | 97.9657 | 86.6351 | 95.9314 | 99.5505 |
| 12 | 96.4130 | 96.7391 | 97.1195 | 94.6195 | 87.5000 | 93.9673 | 82.1739 | 99.4021 |
| 13 | 88.7231 | 86.8802 | 92.4967 | 92.0798 | 89.5787 | 88.2404 | 84.4888 | 97.6305 |
| 14 | 98.1034 | 97.6293 | 95.7435 | 97.5646 | 97.1228 | 96.6810 | 97.5754 | 99.1918 |
| 15 | 90.8450 | 88.0281 | 89.7887 | 83.6267 | 92.9577 | 86.6197 | 85.2112 | 97.3591 |
| 16 | 99.8938 | 98.8222 | 99.4190 | 99.7374 | 99.5702 | 99.9071 | 99.6206 | 99.8328 |
| Para | 1078336 | 1380480 | 15808224 | 836816 | 836816 | 16680662 | 2667408 | 2114128 |
| Train (s) | 69.87 | 86.94 | 119.54 | 308.96 | 309.88 | 3185.62 | 305.70 | 232.86 |
| Test (s) | 9.93 | 10.47 | 10.35 | 58.06 | 53.79 | 384.09 | 57.25 | 52.85 |
| Flops | 2670080 | 18778112 | 15732736 | 110592 | 110592 | 15730688 | 167936 | 1999872 |
| κ | 97.2334 | 96.7964 | 97.9417 | 97.0946 | 97.2897 | 95.7417 | 96.2026 | 99.1413 |
| OA | 97.6367 | 97.2616 | 98.2402 | 97.5179 | 97.6849 | 96.3623 | 96.7568 | 99.2661 |
| AA | 95.1383 | 95.5310 | 97.0987 | 95.0435 | 95.5937 | 92.8650 | 92.9988 | 98.6722 |

The results across both the IP (Table III and Fig 4), HC (Table IV and Fig 5), and HH (Table V and Fig 6) datasets demonstrate that MSST consistently achieves superior performance in terms of per-class accuracy, OA, AA, and κ , outperforming conventional and even recent transformer-based architectures. For instance, MSST achieves the highest OA (99.55%), AA (99.38%), and κ (99.49%) on IP dataset,

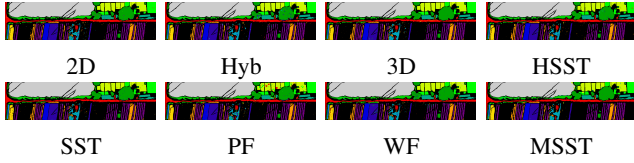


Fig. 5: **HC dataset:** Classification maps, highlighting spatial variability and class-specific performance.

TABLE V: **HH Dataset:** Per-class classification results, along with OA, AA, and κ .

| Class | 2DCNN [23] | HCNN [25] | 3DCNN [24] | HSST [8] | SST [26] | PF [10] | WF [9] | MSST |
|------------------|------------|-----------|------------|----------------|----------------|----------------|----------------|----------------|
| 1 | 98.8461 | 99.4871 | 99.2877 | 98.6324 | 99.7008 | 97.9202 | 99.2877 | 99.8005 |
| 2 | 91.6856 | 92.5968 | 93.9066 | 89.8633 | 88.3826 | 72.3234 | 87.6423 | 98.0068 |
| 3 | 94.3726 | 96.6730 | 98.0661 | 98.2036 | 97.0030 | 97.6079 | 91.9347 | 97.9561 |
| 4 | 99.4941 | 99.6153 | 99.7623 | 99.7403 | 99.4806 | 99.7329 | 99.6852 | 99.8211 |
| 5 | 87.1341 | 86.5873 | 79.0286 | 85.2685 | 91.5406 | 82.1807 | 90.5114 | 94.1138 |
| 6 | 98.2943 | 98.7656 | 98.7252 | 97.5492 | 98.4604 | 97.9487 | 99.2279 | 99.2279 |
| 7 | 86.7988 | 94.0673 | 90.5741 | 95.0215 | 97.0046 | 88.6574 | 95.1128 | 96.8138 |
| 8 | 72.1756 | 65.6635 | 73.6063 | 87.4691 | 80.0690 | 40.4538 | 79.4277 | 98.9639 |
| 9 | 98.7982 | 99.1865 | 98.6319 | 98.5949 | 99.3344 | 97.7999 | 99.1310 | 99.7781 |
| 10 | 90.3985 | 92.7384 | 87.2357 | 90.5599 | 85.3961 | 90.0758 | 86.4934 | 97.9506 |
| 11 | 94.0257 | 90.5574 | 85.7998 | 95.0789 | 95.8234 | 93.4083 | 92.7728 | 93.6081 |
| 12 | 81.5501 | 84.2305 | 89.3902 | 88.9881 | 85.0792 | 89.4125 | 94.7286 | 95.2200 |
| 13 | 91.4252 | 89.1416 | 88.9994 | 94.8995 | 94.0287 | 92.4293 | 87.7376 | 98.1606 |
| 14 | 95.0244 | 95.8401 | 91.5443 | 94.5078 | 97.1179 | 95.7313 | 96.3839 | 93.7466 |
| 15 | 74.6506 | 92.8143 | 84.8303 | 96.0079 | 94.8103 | 88.4231 | 93.4131 | 98.4031 |
| 16 | 97.4662 | 88.9562 | 93.6381 | 94.7948 | 98.1823 | 90.9666 | 99.2564 | 98.7606 |
| 17 | 97.0764 | 95.8803 | 95.9468 | 98.2724 | 92.6245 | 99.4019 | 91.4617 | 99.3355 |
| 18 | 95.0870 | 97.3880 | 95.2736 | 97.0771 | 95.8333 | 99.0671 | 96.3308 | 98.0099 |
| 19 | 94.4903 | 95.5922 | 93.7098 | 96.7860 | 95.0872 | 94.6740 | 97.3829 | 93.1129 |
| 20 | 88.0091 | 91.1072 | 94.7217 | 94.9512 | 97.9345 | 95.9265 | 95.2954 | 99.0820 |
| 21 | 81.9277 | 60.0903 | 73.3433 | 76.9578 | 62.1987 | 38.4036 | 93.2228 | 95.3313 |
| 22 | 77.8712 | 88.6633 | 93.4653 | 97.1782 | 97.5742 | 73.2623 | 95.4455 | 94.5049 |
| Para | 621126 | 922502 | 8928486 | 811478 | 811478 | 9412188 | 2615190 | 817174 |
| Train (s) | 107.14 | 126.55 | 145.88 | 476.38 | 664.13 | 1655.00 | 451.15 | 588.35 |
| Test (s) | 13.31 | 14.87 | 13.96 | 80.85 | 121.23 | 166.06 | 81.53 | 84.47 |
| Flops | 1505248 | 10578688 | 8852992 | 112128 | 112128 | 8850176 | 169472 | 1062400 |
| κ | 94.4348 | 95.1452 | 94.7882 | 96.4281 | 96.2205 | 94.1511 | 95.2651 | 98.1217 |
| OA | 95.5985 | 96.1607 | 95.8835 | 97.1755 | 97.0084 | 95.3772 | 96.2549 | 98.5140 |
| AA | 90.3001 | 90.7110 | 90.8858 | 93.9274 | 92.8485 | 87.0824 | 91.4493 | 97.2595 |

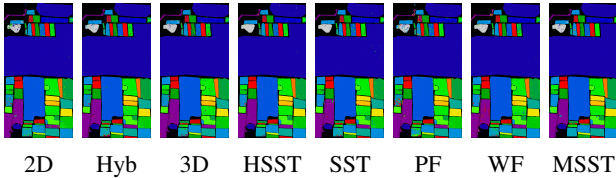


Fig. 6: **HH dataset:** Classification maps, highlighting spatial variability and class-specific performance.

significantly outperforming baseline models. Notably, MSST demonstrates superior performance across most classes, particularly in classes where conventional CNNs and transformers struggle, such as Class 2 (99.30% vs. 97.34% in HCNN) and Class 10 (99.38% vs. 95.68% in HCNN). Additionally, Fig 4 showcases classification maps, highlighting MSST’s ability to capture fine-grained spatial-spectral features with reduced misclassification. Despite its competitive performance, MSST maintains a relatively low parameter count (847,632) and moderate training time (101.64s), striking a balance between efficiency and accuracy.

V. CONCLUSIONS AND FUTURE RESEARCH DIRECTIONS

This work proposed MemFormer, a lightweight and memory-enhanced transformer designed to address the challenges of HSI classification. By integrating a memory-enhanced MHSA mechanism and a memory enrichment strategy, MemFormer effectively reduces information redundancy while capturing intricate spatial-spectral dependencies. Additionally, the SSPE enhances feature expressiveness. Experimental results on benchmark datasets demonstrate that

MemFormer consistently outperforms state-of-the-art methods, achieving superior classification accuracy with significantly fewer parameters. The per-class performance highlights its robustness across diverse land cover categories, and the visualization of classification maps further confirms its ability to preserve spatial structures.

Future work on MemFormer should focus on enhancing its scalability to large hyperspectral datasets with varying spectral resolutions and acquisition conditions. Developing efficient training strategies, self-supervised learning, and domain adaptation techniques will improve generalization and robustness against sensor noise, spectral distortions, and domain shifts. Additionally, optimizing MemFormer for edge computing through model compression will enable real-time applications in UAVs and satellite-based remote sensing. Enhancing interpretability via explainable AI techniques and integrating multi-modal remote sensing data, such as LiDAR and SAR, can further expand its applicability to land cover classification, environmental monitoring, and precision agriculture.

REFERENCES

- [1] M. Ahmad, M. H. F. Butt, A. M. Khan, M. Mazzara, S. Distefano, M. Usama, S. K. Roy, J. Chanussot, and D. Hong, “Spatial-spectral morphological mamba for hyperspectral image classification,” *Neurocomputing*, p. 129995, 2025. [Online]. Available: <https://www.sciencedirect.com/science/article/pii/S0925231225006678>
- [2] Y. Fang, L. Sun, Y. Zheng, and Z. Wu, “Deformable convolution-enhanced hierarchical transformer with spectral-spatial cluster attention for hyperspectral image classification,” *IEEE Transactions on Image Processing*, vol. 34, pp. 701–716, 2025.
- [3] M. Ahmad, S. Shabbir, S. K. Roy, D. Hong, X. Wu, J. Yao, A. M. Khan, M. Mazzara, S. Distefano, and J. Chanussot, “Hyperspectral image classification—traditional to deep models: A survey for future prospects,” *IEEE Journal of Selected Topics in Applied Earth Observations and Remote Sensing*, vol. 15, pp. 968–999, 2021.
- [4] C. Li, B. Zhang, D. Hong, J. Zhou, G. Vivone, S. Li, and J. Chanussot, “Casformer: Cascaded transformers for fusion-aware computational hyperspectral imaging,” *Information Fusion*, vol. 108, p. 102408, 2024.
- [5] L. Huang, Y. Chen, and X. He, “Foundation model-based spectral–spatial transformer for hyperspectral image classification,” *IEEE Transactions on Geoscience and Remote Sensing*, vol. 62, pp. 1–25, 2024.
- [6] Z. Zhao, X. Xu, S. Li, and A. Plaza, “Hyperspectral image classification using groupwise separable convolutional vision transformer network,” *IEEE Transactions on Geoscience and Remote Sensing*, vol. 62, pp. 1–17, 2024.
- [7] M. Ahmad, M. Usama, A. M. Khan, S. Distefano, H. A. Altuwaijri, and M. Mazzara, “Spatial–spectral transformer with conditional position encoding for hyperspectral image classification,” *IEEE Geoscience and Remote Sensing Letters*, vol. 21, pp. 1–5, 2024.
- [8] Q. Yu, W. Wei, D. Li, Z. Pan, C. Li, and D. Hong, “Hypersinet: A synergetic interaction network combined with convolution and transformer for hyperspectral image classification,” *IEEE Transactions on Geoscience and Remote Sensing*, 2024.
- [9] M. Ahmad, U. Ghous, M. Usama, and M. Mazzara, “Waveformer: Spectral–spatial wavelet transformer for hyperspectral image classification,” *IEEE Geoscience and Remote Sensing Letters*, vol. 21, pp. 1–5, 2024.
- [10] M. Ahmad, M. H. F. Butt, M. Mazzara, S. Distefano, A. M. Khan, and H. A. Altuwaijri, “Pyramid hierarchical spatial-spectral transformer for hyperspectral image classification,” *IEEE Journal of Selected Topics in Applied Earth Observations and Remote Sensing*, vol. 17, pp. 17681–17689, 2024.
- [11] S. Jia, Y. Wang, S. Jiang, and R. He, “A center-masked transformer for hyperspectral image classification,” *IEEE Transactions on Geoscience and Remote Sensing*, vol. 62, pp. 1–16, 2024.
- [12] M. Ahmad, M. Mazzara, S. Distefano, A. M. Khan, and S. L. Ullo, “Diffformer: a differential spatial-spectral transformer for hyperspectral image classification,” *IEEE Journal of Selected Topics in Applied Earth Observations and Remote Sensing*, pp. 1–11, 2025.

- [13] L. Sun, H. Zhang, Y. Zheng, Z. Wu, Z. Ye, and H. Zhao, "Massformer: Memory-augmented spectral-spatial transformer for hyperspectral image classification," *IEEE Transactions on Geoscience and Remote Sensing*, vol. 62, pp. 1–15, 2024.
- [14] W.-T. Zhang, Y. Bai, S.-D. Zheng, J. Cui, and Z. zhen Huang, "Tensor transformer for hyperspectral image classification," *Pattern Recognition*, vol. 163, p. 111470, 2025. [Online]. Available: <https://www.sciencedirect.com/science/article/pii/S003132032500130X>
- [15] B. Xi, Y. Zhang, J. Li, T. Zheng, X. Zhao, H. Xu, C. Xue, Y. Li, and J. Chanussot, "Mctgcl: Mixed cnn-transformer for mars hyperspectral image classification with graph contrastive learning," *IEEE Transactions on Geoscience and Remote Sensing*, vol. 63, pp. 1–14, 2025.
- [16] W. Liu, S. Prasad, and M. Crawford, "Investigation of hierarchical spectral vision transformer architecture for classification of hyperspectral imagery," *IEEE Transactions on Geoscience and Remote Sensing*, vol. 62, pp. 1–19, 2024.
- [17] C. Shi, S. Yue, and L. Wang, "Attention head interactive dual attention transformer for hyperspectral image classification," *IEEE Transactions on Geoscience and Remote Sensing*, vol. 62, pp. 1–20, 2024.
- [18] L. Yu, X. Zhang, and K. Wang, "Cmaac: Combining multiattention and asymmetric convolution global learning framework for hyperspectral image classification," *IEEE Transactions on Geoscience and Remote Sensing*, vol. 62, pp. 1–18, 2024.
- [19] R. Chen, G. Vivone, G. Li, C. Dai, D. Hong, and J. Chanussot, "Graph u-net with topology-feature awareness pooling for hyperspectral image classification," *IEEE Transactions on Geoscience and Remote Sensing*, 2024.
- [20] C. Li, B. Zhang, D. Hong, X. Jia, A. Plaza, and J. Chanussot, "Learning disentangled priors for hyperspectral anomaly detection: A coupling model-driven and data-driven paradigm," *IEEE Transactions on Neural Networks and Learning Systems*, 2024.
- [21] P. Kumar Mp, Z.-X. Tu, H.-C. Chen, and K.-C. Chen, "Mitigating negative transfer learning in source free-unsupervised domain adaptation for rotating machinery fault diagnosis," *IEEE Transactions on Instrumentation and Measurement*, vol. 73, pp. 1–16, 2024.
- [22] X. Wan, F. Chen, W. Gao, Y. He, H. Liu, and Z. Li, "Efficient spectral-spatial fusion with multiscale and adaptive attention for hyperspectral image classification," *IEEE Journal of Selected Topics in Applied Earth Observations and Remote Sensing*, vol. 18, pp. 1196–1211, 2025.
- [23] W. Hu, Y. Huang, L. Wei, F. Zhang, and H. Li, "Deep convolutional neural networks for hyperspectral image classification," *Journal of Sensors*, vol. 2015, 2015.
- [24] A. Ben Hamida, A. Benoit, P. Lambert, and C. Ben Amar, "3-d deep learning approach for remote sensing image classification," *IEEE Transactions on geoscience and remote sensing*, vol. 56, no. 8, pp. 4420–4434, 2018.
- [25] M. Paoletti, J. Haut, J. Plaza, and A. Plaza, "A new deep convolutional neural network for fast hyperspectral image classification," *ISPRS journal of photogrammetry and remote sensing*, vol. 145, pp. 120–147, 2018.
- [26] J. Wu, J. Zhao, and H. Long, "Advanced hyperspectral image classification via spectral-spatial redundancy reduction and tokenlearner-enhanced transformer," *IEEE Transactions on Geoscience and Remote Sensing*, vol. 63, pp. 1–12, 2025.